Advances in Transmission Electron Microscopy

Hosson, Jeff Th.M. De; Yasuda, Hiroyuki Y.

Published in:
Self Healing Materials. An Alternative Approach to 20 Centuries of Materials Science

Advances in Transmission Electron Microscopy: Self Healing or is Prevention better than Cure?

Jeff Th.M. De Hosson and Hiroyuki Y. Yasuda

Department of Applied Physics, the Netherlands Institute for Metals Research and Materials science Center, University of Groningen, Nijenborgh 4, the Netherlands
E-mail: j.t.m.de.hosson@rug.nl
Research center for Ultra-High Voltage Electron Microscopy, Osaka University, 7–1, Mihogaoka, Ibaraki, Osaka, 567-0047 Japan
E-mail: hyyasuda@mat.eng.osaka-u.ac.jp

Abstract In the field of transmission electron microscopy fundamental and practical reasons still remain that hamper a straightforward correlation between microscopic structural information and self healing mechanisms in materials. We argue that one should focus in particular on in situ rather than on postmortem observations of the microstructure. In this contribution this viewpoint has been exemplified with in situ TEM nanoindentation and in situ straining studies at elevated temperatures of metallic systems that are strengthened by either solid solution or antiphase boundaries in intermetallic compounds. It is concluded that recent advances in in situ transmission electron microscopy can provide new insights in the interaction between dislocations and interfaces that are relevant for self healing mechanisms in metallic systems.

1 Introduction

Undisputedly microscopy plays a predominant role in unraveling the underpinning mechanisms in autonomic healing phenomena. In general we may say that microscopy is devoted to linking microstructural observations to properties. Nevertheless, the actual coupling between the microstructure studied by microscopy on the one hand and the self healing property of a material on the other is almost elusive. The reason is that these properties are determined by the collective dynamic behavior of defects rather than by the behavior of an individual static defect. However, the situation is not hopeless and in this contribution we argue that for a more quantitative evaluation of the structure–property relationship of self healing material systems extra emphasis on in situ measurements is necessary.

There are at least two reasons that hamper a straightforward correlation between microscopic structural information and autonomic healing properties: one fundamental and one practical reason. Of course it has been realized for a long time that in the field of dislocations, disclinations, and interfaces we are facing nonlinear and

S. van der Zwaag (ed.), *Self Healing Materials. An Alternative Approach to 20 Centuries of Materials Science*, 279–307.

nonequilibrium effects [1, 2]. The defects affected by self healing phenomena are in fact not in thermodynamic equilibrium and their behavior is very much nonlinear. This is a fundamental problem since adequate physical and mathematical bases for a sound analysis of these highly nonlinear effects do not exist. Another more practical reason why a quantitative evaluation of the structure–property relationship of self healing materials is rather difficult has to do with statistics. Metrological considerations of quantitative electron microscopy from crystalline materials put some relevant questions to the statistical significance of microscopy observations. In particular, situations where there is only a small volume fraction of defects present or a very inhomogeneous distribution statistical sampling may be a problem.

The importance of crystalline defects like dislocations lies in the fact that they are the carriers of plastic deformation in crystalline materials. The self healing properties of metallic systems may therefore be tailored by altering the extent to which dislocations can propagate or nucleate cracks. Since metals and alloys are most common in their polycrystalline form, i.e. they consist of many crystals separated by homophase (grain boundaries) or heterophase interfaces, the interaction between dislocations and planar defects is of particular interest. Grain boundaries act as obstacles to dislocation motion as conveyed through the classical Hall–Petch relation [3, 4] describing the increase in yield strength of polycrystalline metals with decreasing obstacle distance. Moreover, with the ongoing miniaturization of devices and materials, length scales have come within reach at which the deformation mechanisms may change drastically. A thorough understanding of such mechanisms is required to improve the mechanical properties of advanced materials and in particular to unravel more quantitatively autonomic healing mechanisms in materials.

As stated before, a major drawback of experimental and theoretical research in the field of crystalline defects is that most of the microscopy work has been concentrated on static structures. Obviously, the dynamics of moving dislocations are more relevant to the deformation mechanisms in metals. To this end we have developed nuclear spin relaxation methods in the past as a complementary tool to TEM for studying dislocation dynamics in metals [5]. A strong advantage of this technique is that it detects dislocation motion in the bulk of the material, as opposed to in situ transmission electron microscopy, where the behavior of dislocations may be affected by image forces due to the proximity of free surfaces. However, information about the local response of dislocations to an applied stress cannot be obtained by the nuclear spin relaxation technique and therefore in situ transmission electron microscopy remains a valuable tool in the study of dynamical properties of defects. Direct observation of dislocation behavior during indentation has recently become possible through in situ nanoindentation in a transmission electron microscope.

To make this contribution consistent and more attractive to study we have chosen to concentrate on the dynamic effects of pile-ups of dislocations interacting with planar defects, homophase as well as heterophase interfaces. The reason is that coplanar dislocation pile-ups may lead to cracks, which should be healed or even better should be prevented from nucleating. To exemplify the advantages and drawbacks of in situ TEM in relation to the interaction between dislocations and interfaces results are

shown of in situ TEM nanoindentations and in situ TEM straining experiments at various temperatures.

The observations are discussed in relation to dynamical response of metallic systems and the influence of dislocations and interfaces on the formation of cracks. The objective of this contribution is not to address various autonomic healing mechanisms in metals but rather to discuss the various recent advances in in situ TEM techniques that can be helpful in attaining a more quantitative understanding of the dynamics of dislocations, interfaces, and cracks. In case of intermetallic compounds some basic ideas about reversible motion of dislocations are presented and discussed. With respect to self healing phenomena, we asked ourselves: is prevention not better than cure?

2 In situ TEM Nanoindentation

The observation of plastic deformation introduced by conventional nanoindentation has been restricted for a long time to postmortem studies of the deformed material, mostly by atomic force microscopy or scanning or transmission electron microscopy. This postmortem approach entails some significant limitations to the analysis of the deformation mechanisms. Most importantly, it does not allow for direct observation of the microstructure during indentation and thus lacks the possibility to monitor deformation events and the evolution of dislocation structures as the indentation proceeds. Moreover, the deformed microstructure observed after indentation is generally different from that of the material under load, due to recovery during and after unloading. In the case of postmortem analysis by transmission electron microscopy, the preparation of the indented surface in the form of a thin foil often leads to mechanical damage to the specimen or relaxation of the stored deformation due to the proximity of free surfaces, thereby further obscuring the indentation-induced deformation.

The recently developed technique of in situ nanoindentation in a transmission electron microscope [6–11], does not suffer from these limitations and allows for direct observation of indentation phenomena. Furthermore, as the indenter can be positioned on the specimen accurately by guidance of the TEM, regions of interest such as particular crystal orientations or grain boundaries can be specifically selected for indentation. In situ nanoindentation measurements [11] on polycrystalline aluminum films have provided experimental evidence that grain boundary motion is an important deformation mechanism when indenting thin films with a grain size of several hundreds of nanometers. This is a remarkable observation, since stress-induced grain boundary motion is not commonly observed at room temperature in this range of grain sizes.

Grain boundary motion in metals typically occurs at elevated temperatures driven by a free energy gradient across the boundary, which may be presented by the curvature of the boundary or stored deformation energy on either side of the boundary [12].

In the presence of an externally applied shear stress, it was found [13] that migration of both low-angle and high-angle grain boundaries in pure Al occurs at temperatures above 200°C. This type of stress-induced grain boundary motion (known as dynamic grain growth) is considered by many researchers to be the mechanism responsible for the extended elongations obtained in superplastic deformation of fine-grained materials. The occurrence of grain boundary motion in room temperature deformation of nanocrystalline fcc metals was anticipated recently by molecular dynamics simulations [14] and a simple bubble raft model [15]. Experimental observations of such grain boundary motion have subsequently been provided by in situ straining experiments of nanocrystalline Ni thin films [16] and in situ nanoindentation of nanocrystalline Al thin films [17]. In both the simulations and the experiments, grain boundary motion was observed for grain sizes below 20 nm. The dislocation mobility is greatly restricted at such grain sizes and other deformation mechanisms become more relevant. In contrast, the grain size for which grain boundary motion was found by in situ nanoindentation [11] was of the order of 200 nm.

In simple deformation modes such as uniform tension or compression, dislocation-based plasticity is still predominant and grain boundary motion generally does not occur. In the case of nanoindentation, however, the stress field is highly inhomogeneous and consequently involves large stress gradients [18]. These stress gradients are thought to be the primary factor responsible for the observed grain boundary motion at room temperature. Since the properties of high purity metals such as pure Al are less relevant for the design of advanced materials, here we focus on the indentation behavior of Al–Mg films and the effect of Mg on the deformation mechanisms described above. To this end, in situ nanoindentation experiments have been conducted on ultrafine-grained Al and Al–Mg films with varying Mg contents [19–21]. The classification “ultrafine-grained” in this respect is used for materials having a grain size of the order of several hundreds of nanometers.

2.1 Stage Design

In situ nanoindentation inside a TEM requires a special specimen stage designed to move an indenter towards an electron-transparent specimen on the optic axis of the microscope. The first indentation holder was developed in the late 1990s by Wall and Dahmen [6, 7] for a high-voltage microscope at the National Center for Electron Microscopy (NCEM) in Berkeley, California. In the following years, several other stages were constructed at NCEM with improvements made to the control of the indenter movement and the ability to measure load and displacement. In the work described in this contribution, two of these stages were used: a homemade holder for a JEOL 200CX microscope [8], and a prototype holder for a JEOL 3010 microscope with dedicated load and displacement sensors, developed in collaboration with Hysitron (Hysitron, Minneapolis, MN, USA).

The principal design of both holders is roughly the same. The indenter tip is mounted on a piezoceramic tube as illustrated in [8]. This type of actuator allows

high-precision movement of the tip in three dimensions, the indentation direction being perpendicular to the electron beam. Coarse positioning is provided by manual screw drives that move the indenter assembly against the vacuum bellows. The indenter itself is a Berkovich-type diamond tip, which is boron-doped in order to be electrically conductive in the TEM. The goniometer of the TEM provides a single tilt axis, so that suitable diffraction conditions can be set up prior to indentation.

The motion of the indenter into the specimen during indentation is controlled by the piezoceramic tube. In the holder for the JEOL 200CX, the voltage applied to the tube is controlled manually and recorded together with the TEM image. Since the compliance of the load frame is relatively high, the actual displacement of the indenter into the material depends not only on the applied voltage, but also to a certain extent on the response of the material. Consequently, this indentation mode is neither load- nor displacement controlled. In the prototype holder for the JEOL 3010 and JEOL2010F, a capacitive sensor monitors the load and displacement during indentation. The displacement signal is used as input for a feedback system that controls the voltage on the piezoceramic tube based on a proportional-integral-derivative (PID) algorithm [22]. The indentation is therefore displacement controlled and can be programmed to follow a predefined displacement profile as a function of time.

The need for a separate load and displacement sensor as implemented in the prototype holder is mainly due to the complex response of the piezo tube. If the response were fully known, the load could be calculated at any time during indentation from the displacement (which can be determined directly from the TEM image) and the characteristics of the load frame [23]. Ideally, the correlation between the applied voltage and the displacement of the piezo element is linear. However, hysteresis and saturation effects lead to significant nonlinearities. Moreover, as lateral motion is achieved by bending the tube, the state of deflection strongly affects the response in the indentation direction as well. Calibration measurements of the piezo response in vacuo at 12 points across the lateral range showed an average proportionality constant of 0.12 $\mu m/V$ with a standard deviation as large as 0.04 $\mu m/V$. Although during indentation, the deflection of the tube is approximately constant and the response becomes more reproducible, the above-mentioned hysteresis and saturation effects still complicate the measurement of the load. The implementation of a dedicated load sensor, as in the new prototype holder, is therefore essential for obtaining reliable quantitative indentation data. Section 2.3 highlights the differences between the in situ indentation load displacement and displacement-controlled holders.

2.2 Specimen Geometry and Specimen Preparation

The geometry of the specimens used for in situ nanoindentation has to comply with two basic requirements: (i) an electron-transparent area of the specimen must be accessible to the indenter in a direction perpendicular to the electron beam; and (ii) this area of the specimen must be rigid enough to support indentation without bending or breaking. A geometry that fulfills both these requirements is a wedge

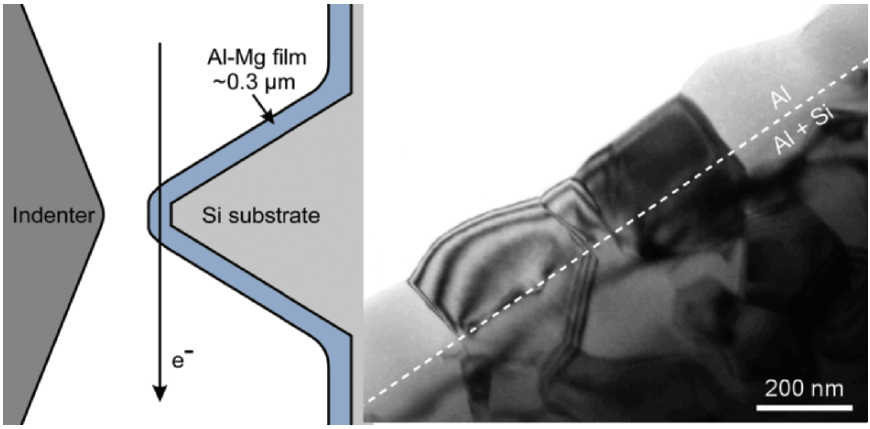

Fig. 1 (**a**) Schematic of in situ TEM indentation setup. The deposited Al–Mg film is electron-transparent and accessible to the indenter at the tip of the Si wedge. (**b**) Typical bright-field image of a deposited film. The dashed line shows the top of the Si ridge

that is truncated to a cap width large enough to provide the necessary rigidity while still allowing the electron beam to pass through. For the present investigation, wedge specimens were used as prepared by bulk silicon micromachining. Using this technique, wedge-shaped protrusions are routinely prepared on Si (001) substrates with a resolution of the order of 1 μm. The side planes of the ridge are aligned with {111} planes of the silicon crystal, so that repeated annealing and oxide removal subsequently leads to sharpening of the wedge driven by a reduction of the surface energy. The silicon ridge specimen geometry provides a means to investigate any material that can be deposited as a thin film onto the silicon substrate. Metals with a low atomic number such as aluminum are particularly suitable for this purpose, since films of these metals can be made to several hundreds of nanometers thickness and still be transparent at the cap of the wedge to electrons with typical energies of 200–300 kV, as schematically depicted in Figure1a. An example of a resulting TEM image is shown in Figure 1b.

The Al and Al–Mg films that will be discussed were deposited by thermal evaporation. The substrate was kept at 300°C to establish a grain size of the order of the layer thickness, which was 200–300 nm for all specimens. After evaporation, the substrate heating was switched off, allowing the specimen to cool down to room temperature in approximately one hour. One pure Al film was prepared by evaporating a high purity (5N) aluminum source. Deposition of the Al–Mg alloy films was achieved by evaporating alloys with varying Mg contents. Since Al and Mg have different melting temperatures and vapor pressures, the Mg content of the deposited film is not necessarily equal to that of the evaporated material. Moreover, the actual evaporation rates depend on the quality of the vacuum and the time profile of the crucible temperature. The composition of the deposited alloy films was therefore determined by energy dispersive spectrometry (EDS) in a scanning electron microscope at 5 kV.

The measured Mg concentrations of the four Al–Mg films prepared were 1.1wt%, 1.8wt%, 2.6wt%, and 5.0wt%.

Since the solubility level of Mg in Al is 1.9wt% at room temperature [24], β' and β precipitates were formed in the 2.6wt% and 5.0wt% Mg specimens due to the relatively long cooling time. The attainable image resolution in the indentation setup was not high enough to resolve these precipitates, being compromised by the thickness of the specimen and possibly by the fact that the electron beam travels very closely to the substrate over a large distance. Nevertheless, the presence of precipitates both in the matrix and at the grain boundaries could be confirmed by strain contrast and distorted grain boundary fringes, respectively, which were not observed in the 1.1wt% and 1.8wt% Mg specimens [20]. Furthermore, the presence of the brittle β phase on the grain boundaries leads to the appearance of intergranular cracks in the 2.6wt% and 5.0wt% Mg specimens. While Al deposited on a clean Si (001) surface may give rise to a characteristic mazed bicrystal structure due to two heteroepitaxial relationships [25], the Si substrates used in the present experiments were invariably covered with a native oxide film. Therefore, the orientations of the Al and Al–Mg grains of the film show no relation to that of the Si surface. An EBSD scan on the evaporated Al film showed a significant $\langle 111 \rangle$ texture, which can be explained by the fact that the surface energy of fcc materials has a minimum for this orientation. Furthermore, the EBSD measurements provided the distribution of the grain boundary misorientations, which showed that the grains are mostly separated by random high-angle grain boundaries with no significant preference for particular CSL orientations.

On each of the evaporated films, three to four in situ experiments were carried out with maximum depths ranging from 50 to 150 nm, using the indentation stage for the JEOL 200CX. The indentation rate, being controlled manually through the piezo voltage, was on the order of 5 nm/s. In addition, several quantitative in situ indentation experiments were conducted with the prototype holder for the JEOL 3010 microscope on the Al and Al–2.6% Mg films. These displacement-controlled indentations were made to a depth of approximately 150 nm with a loading time of 20 s. In order to be able to resolve grain boundary phenomena during each in situ indentation, the specimen was tilted to such an orientation that two adjacent grains were both in (different) two-beam conditions.

2.3 Load Control Versus Displacement Control

The onset of macroscopic plastic deformation during indentation is thought to correspond to the first deviation from elastic response in the load vs. displacement curve. For load-controlled indentation of crystalline materials, this deviation commonly has the form of a displacement burst at constant indentation load [33]. The elastic shear stress sustained prior to this excursion is often much higher than predicted by conventional yield criteria and can even attain values close to the theoretical shear strength, as was initially observed by Gane and Bowden [34]. The physical origin

of the enhanced elastic loading and the subsequent displacement burst has been the subject of extensive discussions in literature [35]. While various mechanisms may be relevant in particular situations, many researchers [36–39], agree that the onset of macroscopic plastic deformation is primarily controlled by dislocation nucleation and/or multiplication, although the presence of an oxide film may significantly affect the value of the yield point.

The initial yield behavior of metals is in some cases characterized by a series of discontinuous yield events rather than a single one [33, 40, 41]. Because of the characteristic steps that result from these yield events during load-controlled indentation, this phenomenon is commonly referred to as "staircase yielding." The excursions are separated by loading portions that are predominantly elastic, and the plasticity is thus confined to the yield excursions at this stage of deformation. Staircase yielding may be explained in terms of the balance between the applied stress and the back stress on the indenter exerted by piled-up dislocations that are generated during a yield event at constant load. When the forces sum to zero, the source that generated the dislocations stops operating, and loading continues until another source is activated. This process repeats until fully plastic loading is established. Bahr et al. [39] suggested that staircase yielding occurs if the shear stress prior to the yield point is only slightly higher than the yield stress, so that upon yielding, the shear stress drops below the nucleation shear stress and further elastic loading is needed to activate the same or another dislocation source. From these viewpoints, the load at which each excursion occurs depends on the availability of dislocation sources under the indenter and on the shear stress required to nucleate dislocations from them. This accounts for the variation that is commonly observed between indentations in the number of excursions and their size.

Whereas extensive staircase yielding occurs during load-controlled indentation of pure Al thin films, it was recently found that Al–Mg thin films show essentially continuous loading behavior under otherwise identical conditions [20]. The apparent attenuation of yield excursions was attributed to solute drag on dislocations. In this contribution the influence of solute Mg on the plastic instabilities in indentation of Al–Mg is reported here in detail. It is shown that the effect of solute drag on the resolvability of discrete yield behavior depends strongly on the indentation parameters, in particular on the indentation mode, being either load- or displacement-controlled.

Conventional ex situ nanoindentation measurements were conducted both under load control and displacement control using a TriboIndenter (Hysitron, Minneapolis, MN) system equipped with a Berkovich indenter with an end radius of curvature of approximately 120 nm. Scanning probe microscopy (SPM) was used to image the surface prior to each indentation to select a target location on a smooth flat area of the specimen away from the wedge. The displacement-controlled experiments were performed at a displacement rate of 10 nm/s; the loading rate in the load-controlled experiments was 10 μN/s, which under the present circumstances corresponds to about 10 nm/s during the first tens of nanometers of loading.

In situ nanoindentation experiments under displacement control were performed in a TEM using a quantitative indentation stage, which has recently been developed and

is described in [40]. The stage was equipped with a Berkovich indenter with an end radius of approximately 150 nm as measured by direct imaging in the TEM. The in situ indentations were carried out on the Al and Al–Mg films at the cap of the wedge, where the surface has a lateral width of the order of 300 nm. The displacement rate during indentation was 7.5 nm/s.

Given the significant rounding of the indenter in both types of experiments, the initial loading is well described by spherical contact up to a depth of the order of 10 nm. In Tabor's approximation, the elastoplastic strain due to spherical loading is proportional to $\sqrt{\delta/R}$, where δ is the indentation depth and R the indenter radius; the equivalent strain rate is therefore proportional to $1/\sqrt{(4\delta R)}\mathrm{d}\delta/\mathrm{d}t$. Using the above-mentioned values it is easily seen that at a depth of 10 nm the initial strain rates in both types of experiments compare reasonably well to one another, with values of $0.14\,\mathrm{s}^{-1}$ and $0.10\,\mathrm{s}^{-1}$ for the ex situ and in situ experiments, respectively.

The load-controlled indentation measurements show displacement bursts during loading on both the Al and the Al–Mg films, as illustrated in Figure 2. The curvature

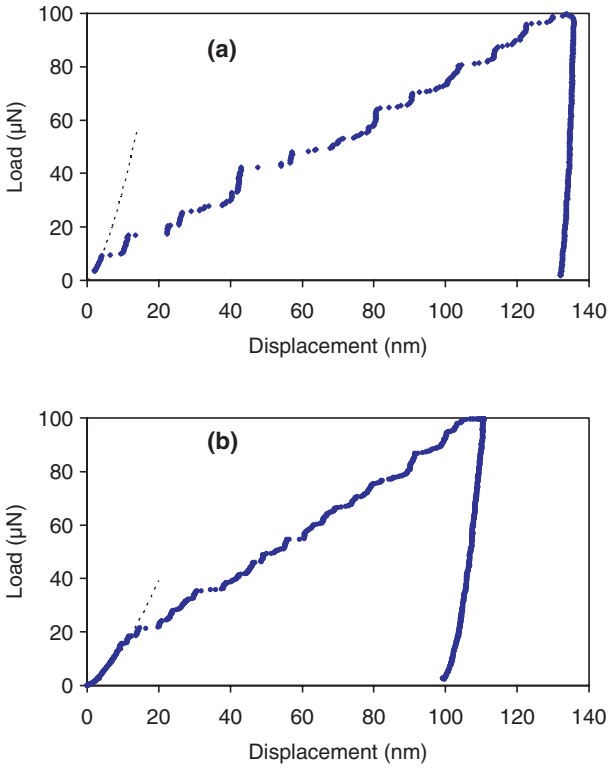

Fig. 2 Ex situ load-controlled indentation response of: (**a**) pure Al and (**b**) Al–2.6% Mg. The dashed lines represent elastic indentation by a spherical indenter with a radius of 120 nm, with the respective elastic moduli calculated from the slope of the unloading curve

of the loading portion prior to the first excursion is well described by elastic Hertzian contact, as indicated by the dashed curves. With the tip radii used, the depth over which the tip is rounded is larger than the depth over which the initial elastic behavior is expected; therefore, the expression for a spherical indenter is used. The subsequent yield behavior is classified as staircase yielding due the aforementioned dislocation-based mechanisms. Staircase yielding has been reported for indentation of both single crystal and ultrafine-grained polycrystalline Al thin films [9, 21] and therefore its occurrence is not expected to depend strongly on the presence of grain boundaries in our case.

The displacement bursts encountered in Al–Mg have a magnitude of up to 7 nm, which is substantially smaller than those observed in pure Al, being up to 15 nm in size. In fact, earlier load-controlled indentation measurements on Al–Mg [20] did not show clearly identifiable discrete yield events whatsoever, due to factors such as lower accuracy of the displacement measurement and more sluggish instrument dynamics with a resonance frequency of only 12 Hz as compared to about 125 Hz in the present instrument. In those experiments, it was observed that the attenuation of displacement bursts occurs for Mg concentrations both below and above the solubility limit in Al, from which it was inferred that the effect is due to solute Mg, which impedes the propagation of dislocation bursts through the crystal. Consequently, at a constant indentation load and for a given amount of stored elastic energy, fewer dislocations can be pushed through the solute atmosphere of Al–Mg than through a pure Al crystal, which accounts for the observed difference in size of the yield excursions. Comparison of Figures 2a and 2b further reveals that the loading portions in between consecutive yield events in Al–Mg show significant plastic behavior, whereas in Al they are well described by elastic loading, which at these higher indentation depths is attested by a slope that is intermediate between spherical [42] and Berkovich [43] elastic contact. The plasticity observed in Al–Mg can be explained in terms of the solute pinning of dislocations that were already nucleated during the preceding yield excursion. As the load increases further, some of the available dislocations are able to overcome the force associated with solute pinning, thereby allowing plastic relaxation to proceed more smoothly. Since dislocation motion is less collective than in pure Al, the measured loading response has a more continuous appearance.

When carried out under displacement control, the ex situ indentations show a much more evident effect of the solute drag on the initial yielding behavior, as illustrated in Figure 3. The loading curves of both Al and Al–Mg show pronounced load drops, which have the same physical origin as the displacement excursions in load-controlled indentation, i.e. stress relaxation by bursts of dislocation activity. Also in this case, the loading behavior up to the first load drop closely follows the elastic response under spherical contact. However, the appearance of the load drops is very different: in pure Al, the load drops are large and mostly result in loss of contact, while in Al–Mg they are smaller and more frequent, and contact is maintained during the entire loading segment. The forward surges occurring with each load drop are a result of the finite bandwidth of the feedback system. In the case of pure Al,

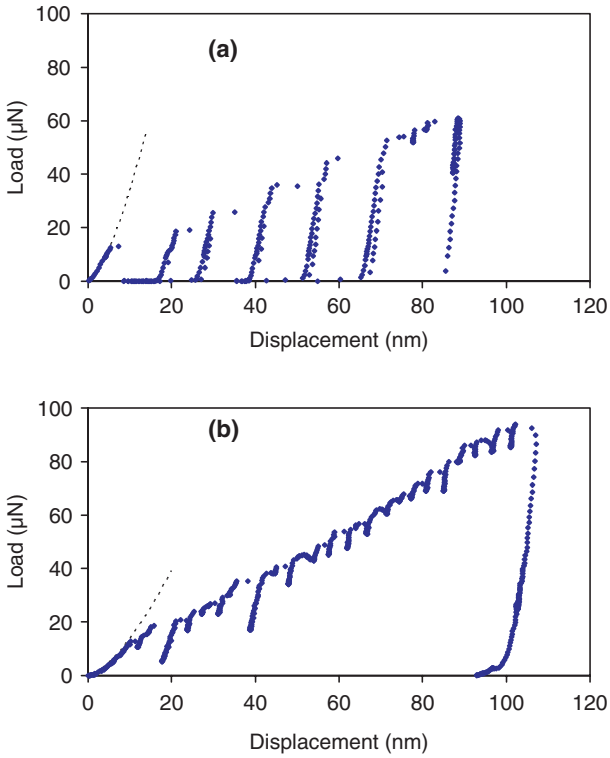

Fig. 3 Ex situ displacement-controlled indentation response of: (**a**) pure Al and (**b**) Al–2.6% Mg

the observations of complete load relaxation and loss of contact are indicative of the stored elastic energy being fully released in the forward surge before the feedback system is able to reduce the load. In Al–Mg however, solute pinning strongly reduces the dislocation velocity, which enables the feedback system to respond fast enough to maintain elastic contact. Thus, not all of the stored elastic energy is inputted back into the specimen.

The comparison between the load-controlled and displacement-controlled experiments shows that discrete yield events are far more resolvable under displacement control. This is particularly the case for solid solution strengthened alloys, in which the somewhat ragged appearance of the loading portions in between clearly identifiable strain bursts in the load-controlled data is clarified as a series of small but easily distinguishable discrete yield events in the displacement-controlled data. This enhanced sensitivity may be rationalized as follows. When the critical shear stress for a dislocation source under the indenter is reached under load control, a discernable strain burst results only if the source is able to generate many dislocations at constant load, i.e. the load-displacement curve must shift from a positive slope to an extended range of zero slope for the slope change to be readily detected. This again is possible

only if the newly nucleated dislocations can freely propagate through the lattice, as in pure Al. Under displacement control however, provided that the feedback bandwidth is sufficiently high, the system may respond to the decrease in contact stiffness when only a few dislocations are nucleated, causing a distinct shift from a positive to a steeply negative slope in the load-displacement curve. Therefore, a detectable load drop can occur without collective propagation of many dislocations and as such may easily be observed even under solute drag conditions. This result cautions against using only load-controlled indentation to determine whether yielding proceeds continuously.

The in situ TEM indentations on both Al and Al–Mg show a considerable amount of dislocation activity prior to the first macroscopic yield point. This is a remarkable observation, as the initial contact would typically be interpreted as purely elastic from the measured loading response. The observations of incipient plasticity are illustrated in Figure 4 by the TEM images and load-displacement data recorded during an in situ displacement-controlled indentation on Al–Mg. While the indented grain is free of dislocations at the onset of loading (Figure 4a), the first dislocations are already nucleated within the first few nanometers of the indentation (Figure 4b), i.e. well before the apparent initial yield point that would be inferred from the load vs. displacement data only. At the inception of the first macroscopic yield event, dislocations are present throughout the entire grain (Figure 4c). The yield event itself is associated with a rearrangement of these dislocations, which significantly changes the appearance of the dislocation structure (Figure 4d). However, the number of newly nucleated dislocations between (c) and (d) is relatively small, as also becomes clear from the limited increase in indentation depth (3 nm corresponds to approximately 10 Burgers vectors). This supports our perception that only a small number of dislocations need to be nucleated in order for a yield event to be detected under displacement control, although the first dislocations nucleated between (a) and (b) do not provide an obvious signature in the load-displacement curve. In the case of in situ displacement-controlled indentation of pure Al [10], the onset of dislocation nucleation/propagation coincides with a barely detectable yet unambiguous load drop that occurs well before the initial macroscopic yield event, which is further evidence of more collective dislocation motion in Al in comparison to Al–Mg. The in situ observations of Al–Mg furthermore provide a self-consistency check for the dynamics of a yield event. With solute drag preventing full load relaxation, the size of a forward surge Δh is essentially determined by the dislocation velocity v and the mechanical bandwidth of the transducer f. Therefore, ignoring the drag exerted by the feedback system, the dislocation velocity may to a first approximation be estimated as $v \sim \Delta h \cdot f$, which, using $\Delta h = 7\,\mathrm{nm}$ and $f = 125\,\mathrm{Hz}$, yields a velocity of the order of $1\,\mu\mathrm{m/s}$. This is of the same order as observed in situ for the initial dislocations in Figure 4b, which traversed the 300 nm film thickness in about 130 ms (four video frames at a frame rate of 30 frames per second, see video at http://www.dehosson.fmns.rug.nl/).

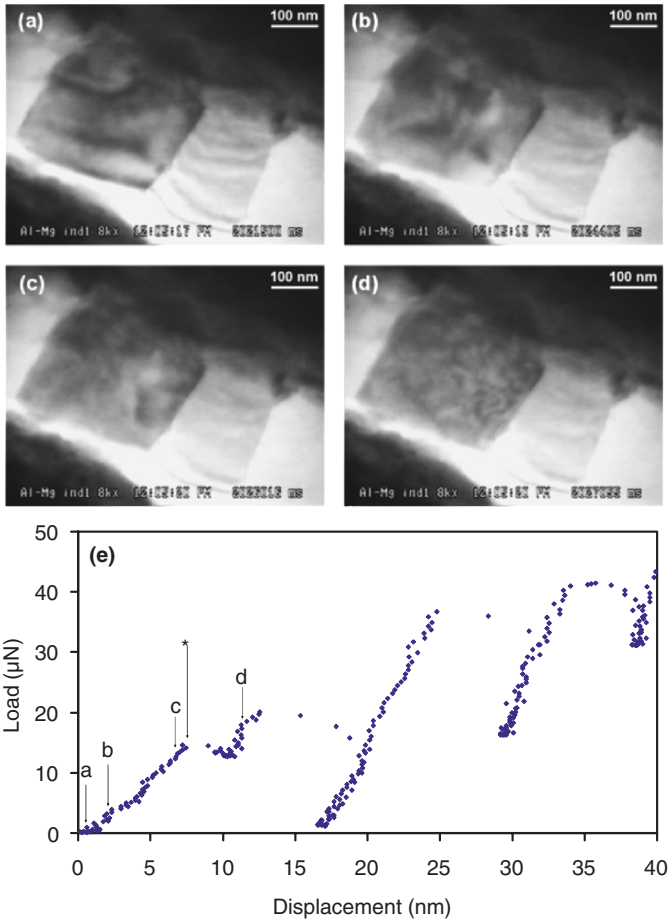

Fig. 4 TEM bright-field Image sequence (**a**–**d**) from the initial loading portion; (**e**) of the indentation on Al–2.6% Mg depicted in Figure 9b. The first dislocations are nucleated between (**a**) and (**b**), i.e. prior to the apparent yield point. The nucleation is evidenced by an abrupt change in image contrast: before nucleation, only thickness fringes can be seen, whereas more complex contrast features become visible at the instant of nucleation. (See http://www.dehosson.fmns.rug.nl/.)

2.4 Dislocation and Grain Boundary Motion

The effect of Mg on the propagation of dislocations is particularly visible during the early stages of loading. While in pure Al the dislocations instantly spread across the entire grain (i.e. faster than the 30 frames per second video sampling rate), they advance more slowly and in a jerky type fashion in all observed Al–Mg alloys. Figure 5 shows a sequence of images from an indentation in Al–2.6% Mg. The arrows mark the consecutive positions where the leading dislocation line is pinned by solutes. From these images, the mean jump distance between obstacles is estimated

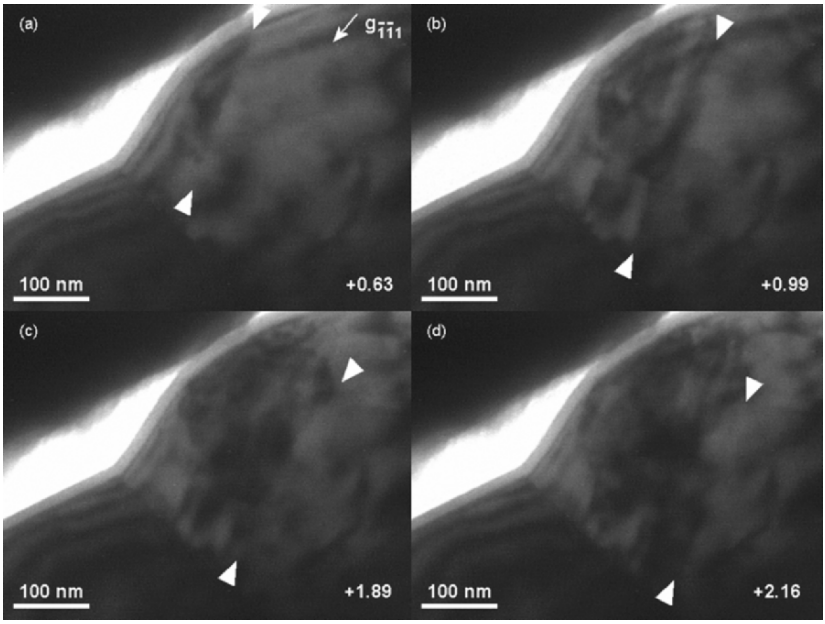

Fig. 5 Series of bright-field images showing jerky motion of dislocations during indentation of Al–2.6wt% Mg. The time from the start of the indentation is given in seconds. Note the presence of a native oxide layer on the surface

to be of the order of 50 nm. Due to the single-tilt axis limitation of the indentation stage, the orientation of the slip plane relative to the electron beam is unknown; therefore, the measured jump distance is a projection and a lower bound of the actual jump distance.

At the low strains for which jerky-type dislocation motion is observed, solute atoms are the predominant barriers to mobile dislocations, as has been shown in earlier in situ pulsed nuclear magnetic resonance (NMR) experiments [5, 26–28]. Consequently, the mean jump distance can be predicted by Mott–Nabarro's model of weakly interacting diffuse forces between Mg solutes and dislocations in Al [27]. A calculation of the effective obstacle spacing, assuming that the maximum internal stress around a solute atom has a logarithmic concentration dependence, yields a value of 30 nm in Al–2.6% Mg. This is in fair agreement with our experimental observation of a mean jump distance of the order of 50 nm.

Besides solute atoms, (semi-) coherent β'/β precipitates in Al–Mg alloys can also provide significant barriers to dislocation motion. As aforementioned, the mean spacing of these precipitates could not be measured very accurately due to the limited resolution of the microscope combined with the specific indentation stage. However, we can make an estimate based on the solid solubility of Mg in Al at room temperature of 1.9wt%. The calculated volume fraction f_V is 2.4% for the β phase at 300K. The mean planar separation, which is a relevant measure for the interaction of

a gliding dislocation with a random array of obstacles in its slip plane, is given by [30, 31]

$$\lambda \cong \frac{2\sqrt{2}\pi r}{3 f_V} \tag{1}$$

provided that the size of the particles r is negligible in comparison with their center-to-center separation, i.e. if $\lambda >> r$. It is reasonable to assume that the minimum size of the semicoherent precipitates is at least 10 nm to produce sufficient strain contrast. As a result, the mean planar separation of the precipitates is calculated to be at least 92 nm, i.e. larger than the mean separation between the solutes. In this approach, the obstacles are assumed to be spherical and consequently, we ignore the effect that the precipitation in Al may become discontinuous or continuous depending on the temperature. However, even in the case of a Widmanstätten structure, the effective separation between the needle-shaped precipitates is larger than the effective solute obstacle spacing [32]. Therefore, based on the experimental observations in the alloys below and above the solid solubility of Mg, the strain contrast and the abovementioned theoretical considerations, solute atoms are assigned as the main obstacles to dislocation motion.

To confirm the occurrence of grain boundary movement in aluminum as had been reported earlier [11], several in situ indentations were performed near grain boundaries in the pure Al film. Indeed, significant grain boundary movement was observed for both low- and high-angle boundaries. It should be emphasized that the observed grain boundary motion is not simply a displacement of the boundary together with the indented material as a whole; the boundary actually moves through the crystal lattice and the volume of the indented grain changes accordingly at the expense of the volume of neighboring grains. The trends observed throughout the indentations suggest that grain boundary motion becomes more pronounced with decreasing grain size and decreasing distance from the indenter to the boundary. Moreover, grain boundary motion occurs less frequently as the end radius of the indenter increases due to tip blunting or contamination. Both these observations are consistent with the view that the motion of grain boundaries is promoted by high local stress gradients as put forward in the introduction of this paper. The direction of grain boundary movement can be both away from and towards the indenter, and small grains may even completely disappear under indentation [17]. Presumably, the grain boundary parameters play an important role in the mobility of an individual boundary, since the coupling of the indenter-induced stress with the grain boundary strain field depends strongly on the particular structure of the boundary.

The quantitative in situ indentation technique offers the possibility to directly relate the observed grain boundary motion to features in the load-displacement curve. While this relation has not been thoroughly studied in the present investigation, preliminary results suggest that the grain boundary motion is associated with softening in the loading response. Softening can physically be accounted for by the stress relaxation that occurs upon grain boundary motion. However, the quantification of overall mechanical behavior is complicated by the frequent load drops at this stage of indentation, and further in situ indentation experiments are needed to investigate

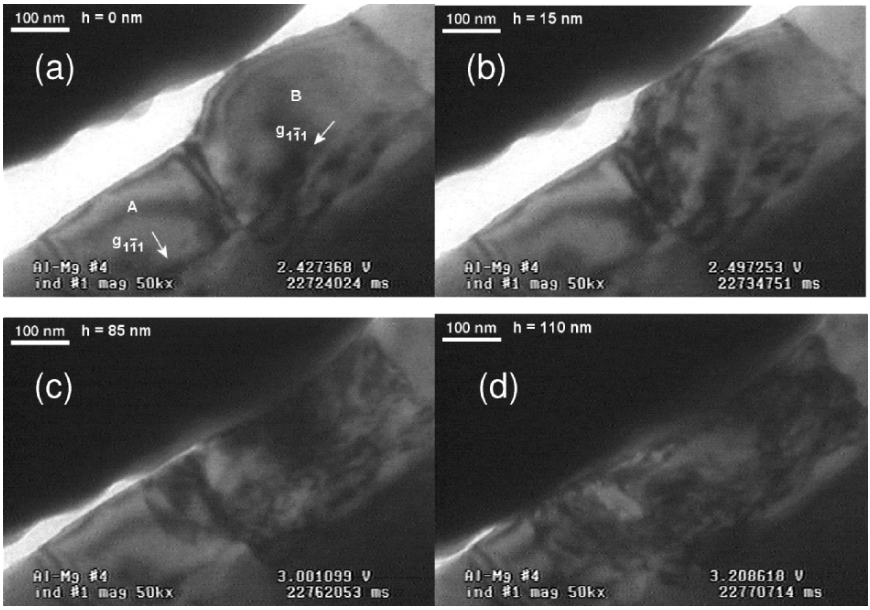

Fig. 6 Series of bright-field images from an indentation on Al–1.8% Mg. No movement of the high-angle grain boundaries is observed

this phenomenon more systematically and quantitatively. The movement of grain boundaries as observed in Al was never found for high-angle boundaries in any of the Al–Mg specimens, even when indented to a depth greater than half of the film thickness (see Figure 6). Our observations as such indicate a significant pinning effect of Mg on high-angle grain boundaries in these alloys. In contrast to high-angle grain boundaries, the mobility of low-angle boundaries in Al–Mg was found to be less affected by the presence of Mg.

The Al–Mg films investigated include compositions both below and above the solubility limit of Mg in Al. However, no differences in indentation behavior between the solid solution and the precipitated microstructures were observed. Consequently, the observed pinning of high-angle boundaries in Al–Mg is attributed to solute Mg. The pinning is presumably due to a change in grain boundary structure or strain fields caused by solute Mg atoms on the grain boundaries.

Relatively few direct experimental observations have been reported of this type of interaction. Sass and coworkers observed that the addition of Au and Sb impurities to bcc Fe changes the dislocation structure of ⟨100⟩ twist boundaries of both low-angle [44] and high-angle [45] misorientation. Rittner and Seidman [46] calculated solute distributions at ⟨110⟩ symmetric tilt boundaries with different boundary structures in an fcc binary alloy using atomistic simulations. However, the influence of solutes on the structure of such boundaries has not been experimentally identified.

The fact that low-angle grain boundaries were found to be mobile regardless of the Mg content can be explained by their different boundary structure. Up to a

misorientation of 10–15°, low-angle boundaries can be described as a periodic array of edge and screw dislocations by Frank's rule [47]. In such an arrangement, the strain fields of the dislocations are approximated well by individual isolated dislocations and their interaction with an external stress field can be calculated accordingly. Since there is no significant interaction between the individual grain boundary dislocations, the stress required to move a low-angle boundary is much lower than for a high-angle boundary. Low-angle pure tilt boundaries consisting entirely of parallel edge dislocations are fully glissile and therefore particularly mobile. In general, a combination of glide and climb is required to move a low-angle boundary [48]. As a corollary, the structural difference between low and high-angle boundaries also affects the extent of solute segregation. Because solutes generally segregate more strongly to high-angle boundaries [49], the observed difference in mobility may partly be a compositional effect. As aforementioned grain boundary motion is regarded as an essential mechanism in superplastic behavior of metals and that will be the topic of the following section, focusing on in-situ TEM straining-heating experiments.

3 In situ TEM Straining and Heating: Superplasticity

Although initial experimental observations of superplasticity in metals date back to the 1920s, for a long time the phenomenon was mainly regarded as a laboratory curiosity [49]. However, research interests in superplasticity greatly increased in the 1960s [51, 52], when it was demonstrated that in this regime metal sheets could easily be formed to complex shapes. Research efforts are increasingly being directed towards new classes of superplastic materials, some of which exhibit superplastic behavior at considerably higher forming rates [53, 54]. This so called high-strain-rate superplasticity is expected to receive broad industrial interest and may replace existing forming techniques if such materials can efficiently be produced on a large scale [55].

The hallmark of superplastic deformation is a low flow stress σ that shows a high strain rate sensitivity m. A high-strain-rate sensitivity is necessary to stabilize the plastic flow so as to avoid necking during tensile deformation. The incipient formation of a neck leads to a local increase of the strain rate, which, in the case of a positive strain rate sensitivity, leads to an increase of the flow stress in the necked region. If the strain rate sensitivity is sufficiently high, the local flow stress increases to such an extent that further development of the neck is inhibited. Most common metals show a strain-rate sensitivity exponent lower than 0.2, whereas values around 0.3 or higher are needed to delay necking long enough to produce the strains characteristic of superplasticity. Besides a high-strain-rate sensitivity, a low rate of damage accumulation (e.g. cavitation) is required to allow large plastic strains to be reached.

For coarse grained Al–Mg alloys deformed in the viscous glide regime, values for the maximum strain in excess of 300% can be obtained [56, 57, 58]. Such elongations are close to those found in conventional superplasticity of fine-grained Al–Mg alloys

and are sufficient for many practical applications. Moreover, forming by viscous-glide controlled creep has two important advantages over conventional superplastic forming: (i) the rate of viscous glide is not restricted by dislocation climb and consequently higher strain rates can be achieved, and (ii) since viscous glide is independent of grain size, the preparation of the materials is less complex. It should be noted that since the deformation under viscous-glide control does not follow the original definition of superplasticity in the strictest sense, the deformation behavior has also been referred to as "enhanced ductility" or "quasi-superplasticity" by some researchers [56, 57, 59]. There are two competing mechanisms in the viscous-glide regime, dislocation glide and climb; the slower of the two is rate controlling. A physical interpretation of the empirically found three-power-law relation for viscous-glide creep is readily based on the Orowan equation, relating the macroscopic strain rate $\dot{\varepsilon}$ to the mobile dislocation density ρ_m and the average dislocation velocity $\bar{v}_d$. Although no direct measurements of the relation between applied stress and dislocation velocity under solute-drag conditions are available, most models suggest that $\bar{v} \propto \sigma$ in this regime, i.e. the stress exponent $n_v = 1$ [2, 60]. Furthermore, experimental observations have shown that the stress exponent n_d of the mobile dislocation density $\rho_m \propto \sigma^{n_d}$ lies between 1.6 and 1.8 for Al–Mg alloys [2, 60, 62]. This is in reasonable agreement with theoretical predictions [63] suggesting that $\rho_m \propto \sigma^2$ [64]. The strain rate sensitivity index depends critically on the stress dependence of the product $\rho(\sigma)\bar{v}_d(\sigma)$. Assuming $n_v \approx 1$ and $n_d \approx 2$, it follows from the Orowan equation that $\dot{\varepsilon} \propto \sigma^3$, as also is found in the model by Weertman [63]. It follows that the stress exponent $n \approx 3$ and hence, the strain rate sensitivity $m = 1/n \approx 0.33$. From the abovementioned considerations it is clear that the three-power law ($m = 0.33$) is no more than an approximate relationship arising from the stress dependence of the dislocation density and the drag stress.

The alloys presented here are two coarse grained Al–4.4% Mg and Al–4.4% Mg–0.4% Cu alloys with minor amounts of Ti, Mn, and Cr (<0.1%) and an average initial grain size of 70 μm, and a fine grained Al–4.7% Mg–0.7% Mn alloy (AA5083) with an average grain size of 10 μm. (see also [65, 66]). In order to directly observe the evolution of dislocation structures during superplastic deformation, the coarse-grained Al–Mg alloys were subjected to in–situ TEM tensile experiments at elevated temperature in a TEM. Such experiments require a specimen stage that is capable of straining TEM specimens while maintaining a controllable temperature of the order of 400°C. At present, only one type of stage with combined heating and straining capability is commercially available (Gatan, Pleasanton, CA). The design of this stage relies on direct physical contact between a heating element and the specimen to control the specimen temperature. The temperature of the specimen is tacitly assumed to be equal to the furnace temperature as measured by a thermocouple. This is approximately valid at high temperatures (∼1, 000°C) when the specimen is mostly heated by radiation. However, at the intermediate temperatures used in this study, radiation is negligible, and the specimen temperature can only reach the furnace temperature if the thermal contact between the two is very good. The requirement that the specimen be movable for tensile testing results in poor thermal contact; moreover, the degree of contact fluctuates during the course of a tensile experiment.

This was confirmed by calibration measurements in low vacuum on TEM tensile specimens with a thermocouple spot-welded close to the electron-transparent area. Applying a thermally conductive paste between the heating element and the specimen greatly improved the performance of the holder. However, such viscous agents are not suitable for high vacuum systems such as TEMs.

A few homemade heating–straining stages have been developed over the last two decades [67–70], most of which use a filament to heat the specimen by radiation [67, 68]. The temperature is measured by a thermocouple that is positioned as close as possible to the observed area of the specimen. Since the specimen is heated exclusively by radiation, the thermocouple attains approximately the same temperature as the specimen and therefore provides a very accurate temperature measurement. The high temperature in situ experiments reported in this paper were partially conducted at the Institut National Polytechnique in Grenoble, France, using the double tilt heating straining holder described in reference [68]. Calibration experiments have shown the measured temperature of this holder to be accurate to within 10°C [71]. In the intermediate temperature range (∼150°C), in situ tensile experiments were also performed using the Gatan heating straining holder described above.

Figure 7 shows three micrographs representative of the microstructural evolution observed during superplastic forming of the coarse grained Al–Mg alloy. At a strain of a few percent, just beyond the yield point, random configurations of dislocations are visible (Figure 7a). This stage of deformation is characterized by a drop of the flow stress [72], which indicates dislocation multiplication from an initially low dislocation density pinned by Mg solutes [55]. During further straining, subgrain formation occurs primarily along the original grain boundaries, as in Figure 7b showing subgrain boundaries near a high-angle boundary triple junction. At this stage, the substructure shows many incomplete subgrain boundaries, i.e. boundaries with a very low misorientation ($<1°$) that do not fully enclose a subgrain. Only when a strain of the order of 1 is attained, the subgrains completely fill the grain interior. Figure 7c shows the refined subgrain structure at a strain of 170% and an average subgrain size of approximately 5 μm. Note that the size distribution is fairly broad, with observed subgrain sizes ranging from 1 to 10 μm. [72–75]

The effect of the Mg content on the tensile ductility is twofold. On the one hand, a higher Mg content increases the extent of solute drag, thereby stabilizing the plastic flow. However, beyond a few percent Mg, the effect on the strain-rate sensitivity becomes fairly marginal [57]. On the other hand, the presence of Mg significantly reduces dynamic recovery as evidenced by the slow formation of subgrains. As a result, Mg concentrations above 5% can easily give rise to dynamic recrystallization within a certain domain of temperature and strain rate, which in the absence of grain refining second phase particles leads to rapid coarsening of the microstructure. The currently used composition with 4.4% Mg appears to be a good balance between solute drag and dynamic recovery, leading to enhanced tensile ductility in excess of 300%. In torsional deformation, where a high strain rate sensitivity to avoid necking is less important, the ductility benefits most from dynamic recovery (leading to geometric dynamic recrystallization at high strains) and is consequently higher for pure Al than for Al–Mg alloys [76].

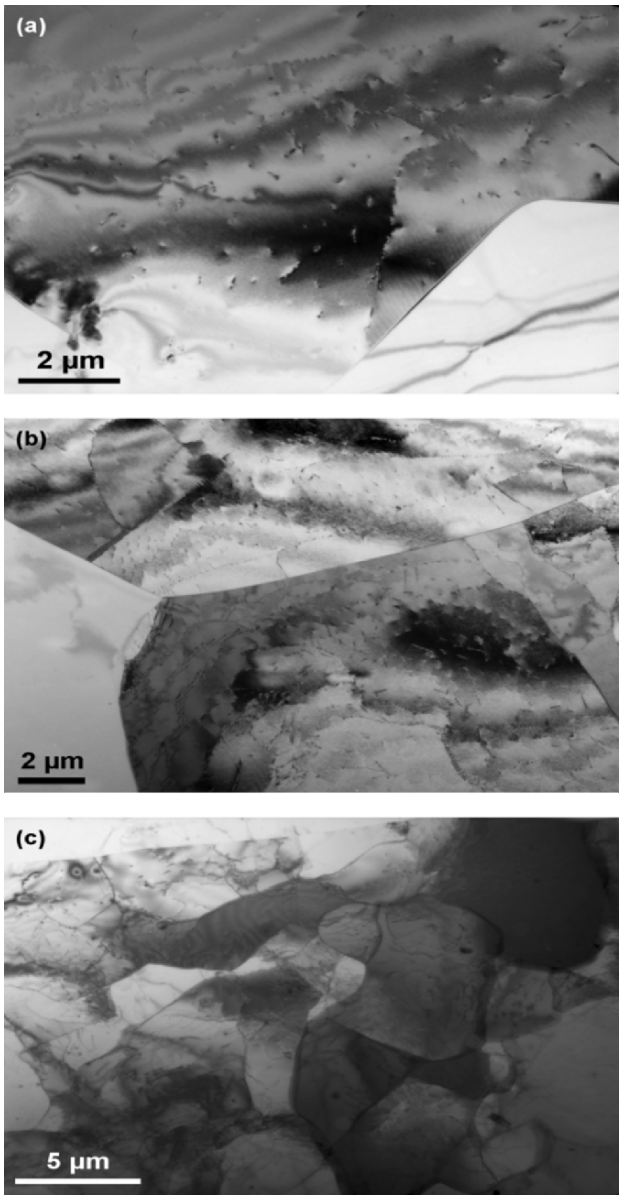

Fig. 7 Dislocation substructure in Al–Mg deformed at 440°C and $5 \cdot 10^{-3}$ s^{-1} to (**a**) 4%; (**b**) 20%; and (**c**) 170%

The initially inhomogeneous formation of subgrains gives rise to a "core and mantle" microstructure, in which most deformation is concentrated along the grain boundaries. In fine-grained superplasticity, this type of microstructure has been associated with grain mantle deformation processes as an accommodating mechanism for grain boundary sliding [73, 74, 77]. In the present case, dynamic recovery is initially confined to the mantle region, but extends throughout the microstructure at higher strains. The evolution of the dislocation substructure during superplastic deformation can be directly observed by in situ tensile experiments in a TEM. A difficulty inherently associated with this technique is presented by the image forces resulting from the proximity of free surfaces, which may significantly influence the dislocation dynamics compared to bulk behavior (e.g. [69]). In the present investigation we have attempted to minimize such effects by preparing tensile TEM specimens from macroscopically prestrained alloys and studying only the initial motion of dislocations from their starting configuration. However, for the present case of Al–Mg alloys, it turns out that surface diffusion of Mg severely limits the temperature range at which the in–situ experiments can be conducted.

At temperatures in excess of 200°C, the tensile TEM specimens were consistently found to fracture intergranularly at very low loads (typically ∼30 gf). This is evidently not representative of the bulk behavior at high temperature showing very high tensile ductility. Below 200°C, the specimens showed ductile transgranular failure at loads of the order of 300 gf. By EDS and electron diffraction analysis it was found that the intergranular fracture areas of the TEM specimens deformed at high temperature contained large amounts of Mg and MgO. Presumably, surface diffusion of Mg becomes appreciable at high temperature and leads to segregation of Mg to the grain boundaries and consequently to grain boundary embrittlement.

In the temperature range below 200°C, dislocation climb is not activated and therefore extensive dynamic recovery is not to be expected. However, even at low temperature, some rearrangements of the substructure were observed that may be illustrative of those occurring during dynamic recovery. The absorption of dislocations by a subgrain boundary is shown in Figure 8; this process contributes to the increase in grain boundary misorientation that is associated with dynamic recovery. In other

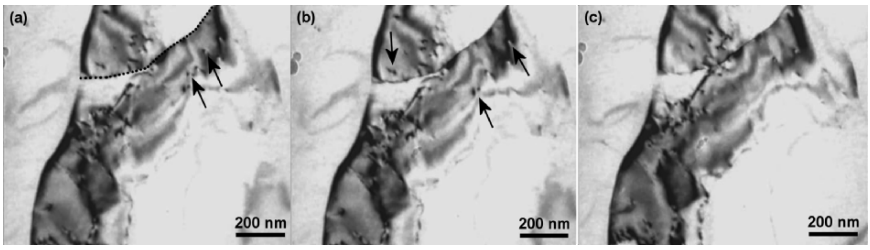

Fig. 8 Absorption of dislocations into a subgrain boundary in Al–Mg during in situ straining at ∼150°C. The subgrain boundary is marked by a dotted line in (**a**). The arrows in (**a**) and (**b**) indicate the dislocations that are absorbed by the boundary in the next image respectively

words: although dislocation motion is solely due to glide at low temperatures, the observed rearrangements resemble the processes that contribute to dynamic recovery at high temperature.

4 In situ TEM Straining: Pseudo-Elasticity

Since dislocations are the basic carriers of plasticity in crystalline materials and fracture is due to crack propagation, one may also expect a relationship between cracks and dislocations. Since dislocations represent discontinuities in displacement, they can also be used, at least in a mathematical sense, to describe a macroscopic static crack and its dynamic behavior. At the same time dislocations facilitate crack opening and relaxation effects and altogether dislocations can be considered as the basic building block of a crack. The idea that a crack can be thought of as an array of discrete coplanar and parallel dislocations was worked out mathematically by Eshelby et al. [78]. Leibfried [79] suggested a continuum approximation and instead of dealing with a coplanar row of discrete dislocations, it was proposed that the crack plane contains a dislocation density smeared out over the crack plane [80]. The stress field of a crack running from $-a$ to a can then simply be related to the stress fields of individual dislocations and via the dislocation distribution $B(x_1)$ on the crack plane ($x_2 = 0$) by integration

$$\sigma_{ij}^{\text{crack}}(x_1, x_2) = \int_{-a}^{a} B(x_1')\sigma_{ij}^{\text{dis}}(x_1 - x_1', x_2)\mathrm{d}x_1' \tag{2}$$

However, close to the crack tip these stresses are above the yield stress of the material. As a consequence plastic flow due to dislocations around the crack-tip region continues until the stress singularity is removed, either by the stresses of the dislocations created during plastic flow, or by blunting of the crack tip due to the emission of dislocations. Mathematically, the pile-up of dislocations produces an infinite stress at the crack tip that can be avoided by abandoning linear continuum mechanics in the tip region [81]. In terms of dislocation theory, the nonlinearity can be dealt with quite simply by allowing some of the leading dislocations in the pile-up to leak away forward into the material ahead of the crack [82].

Besides the conversion of a pile-up of climb and glide edge dislocations into a crack (mode I and mode II, respectively) another feature that can occur is that a grain boundary represented by a wall of stacked edge dislocations is forced apart by an effective shear stress resulting in a crack (see Fig. 9 [83]). This situation of crack nucleation by dislocation pile-ups was analyzed theoretically by Frank and Stroh [84, 85, 86] both for isotropic and anisotropic media. With respect to the topic of autonomic healing, i.e. healing of existing cracks that may propagate, one may ask what should one do for preventing crack formation in the first place. Would not

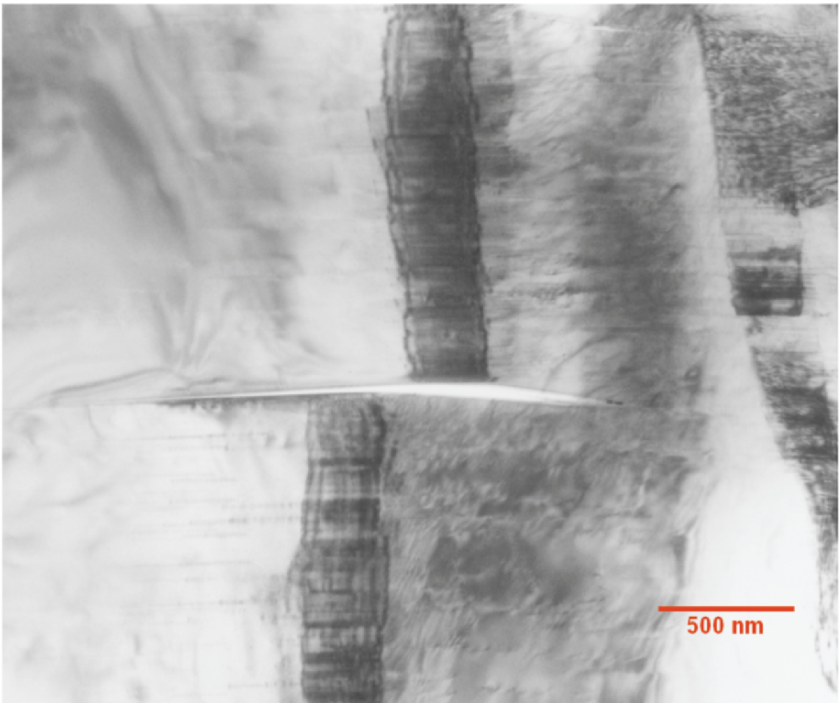

Fig. 9 Stroh crack: a tilt grain boundary is forced apart resulting in a crack. TEM image of a kink band viewed along the $\langle 11\bar{2}0 \rangle$ direction in Ti_3SiC_2

prevention better than cure? The answer for ordered intermetallic compounds under cyclic loading is rather simple. Based on the above considerations about similarities between cracks and dislocations and with reference to sections 2 and 3, an interesting strategy is to avoid extensive dislocation pile-up formation and to make sure that the dislocation slip path is fully reversible so that cracks will not nucleate. In a sense the macroscopic mechanical behavior will look fully elastic although it is based on plasticity. Therefore the phenomenon can be coined pseudo-elasticity, although in literature pseudo-elasticity is linked to a thermoelastic transformation. Here we mean "plasticity induced pseudo-elasticity" [87–90].

Clearly, what is needed for this pseudo-elasticity phenomenon is a low friction stress and a high back stress on dislocations. In pure metals and solid solution strengthened metals pseudo-elasticity (see sections 2 and 3) will not occur because the friction stress τ_o is rather high in bcc metals (about 80% of the flow stress) and a considerable back stress is not available. In ordered compounds the situation is completely different. Because of the translational invariance of the Burgers vector the dislocations move as superlattice dislocations, i.e. as superpartials that are bound by an antiphase boundary energy. The latter provides a back stress τ_{APB} on the

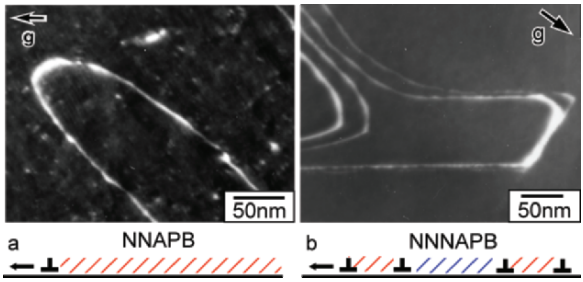

Fig. 10 Dislocation structure in Fe–Al-ordered single crystals (**a**) Fe–23 atom % Al deformed to $\varepsilon_p = 5.0\%$. Superpartials are pulled back by γ NN APB; (**b**) Fe–28 atom % Al deformed to $\varepsilon_p = 0.5\%$. No pseudo-elasticity because of absence of a back stress

leading superpartial dislocation. For the loading τ_l and unloading τ_u situation the balance of stresses reads:

$$\tau_\ell = \tau_0 + \tau_{APB} \tag{3}$$

$$\tau_u = \tau_{APB} - \tau_0 \tag{4}$$

If all the superpartials constituting the superlattice dislocations move, $\tau_\ell = \tau_0$ and no pseudo-elasticity will be observed (see Figure 10). Therefore, pinning of the leading partial is necessary by an obstacle that is strong enough to prevent shearing by the full superlattice dislocation. Ordered compounds provide these obstacles via ordered domains. For example, $D0_3$ ordered compounds like Fe_3Al contains B2 domains. The unit superdislocation in the case of $D0_3$ consists of four $1/4\langle 111\rangle$ partial dislocations. In the $D0_3$ structure this type of superlattice dislocation creates two types of shear APBs. The domains are bound by the inner two superpartial dislocations that are flanked by two $1/4\langle 111\rangle$ APBs on both sides. In the latter case the corresponding APB energy or rather the APB drag tension is formulated as:

$$\gamma_{NN} = \frac{2\sqrt{2}}{a_0^2}\left\{4V_1S_1^2 + V_2\left(S_2^2 - 4S_1^2\right)\right\} \tag{5}$$

whereas the former APB tension on the superpartial is written as:

$$\gamma_{NNN} = \frac{2\sqrt{2}}{a_0^2}\left\{2V_2S_2^2\right\} \tag{6}$$

Here: S_1 is the first-neighboring order parameter, S_2 is the second-neighboring order parameter; V_1 represents the first-neighboring energy; V_2 is the second-neighboring energy, a_0 is the lattice parameter and b represents the magnitude of the Burgers vector. Obviously S_i depends on the chemical composition and temperature but one may infer that the back stress τ_{APB} on the leading partial is larger than on the second partial dislocation, i.e. causing a better recovery ($\gamma_{NN} > \gamma_{NNN}$). If the leading $1/4\langle 111\rangle$ crosses a B2 domain boundary a step is created with a high energy that effectively

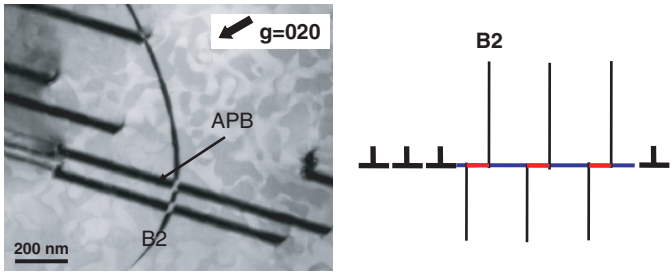

Fig. 11 TEM observation and schematic representation of the intersection between a leading $1/4\langle 111\rangle$ superpartial dislocation in $D0_3$ Fe–Al system and a B2-type domain creating a high-APB energy step

will block the passage of the trailing three superpartials in its wake (see Figure 11). Upon unloading the superpartials are pulled back by the high APB drag tension and a full recovery will be achieved. Indeed pseudo-elasticity was observed in Fe_3Al single crystals with the $D0_3$ crystallographic structure, but interestingly without a martensitic transformation [87–90]. Also Fe_3Ga single crystals with the $D0_3$ structure showed pseudo-elasticity without a martensitic transformation [88]. Recently we have observed emitting dislocations from a crack tip with in situ TEM straining and indeed the fully reverse motion upon unloading provides evidence for the theoretical explanation of pseudo-elasticity, i.e. not based on martensitic transformations but on the motion of partial dislocations comprising superlattice dislocations.

Nevertheless, the details of this mechanism of "prevention is better than cure" approach are not clear. There are several interesting questions about the proposed mechanism. Many dislocations ($\sim 10^{13}$ m^{-2}) have to move to achieve a considerable plastic strain. How do they interact and what is the mean jump distance of the individual or grouped superlattice dislocations? If the dislocations cross-slip, can they move backwards during unloading or are low-energy dislocation structures generated? Pseudo-elastic behavior depends strongly on loading axis and grain boundary engineering is needed for polycrystalline material. Further, it is important whether shear deformation occurred in the twinning or anti-twinning sense, since the $D0_3$ structure is based on bcc.

5 Conclusions and Outlook

This contribution highlights recent advances in transmission electron microscopy, in particular concentrating on in situ TEM experiments. The objective of this contribution is not to address various self healing mechanisms in metals but rather to discuss the various recent advances in in situ TEM techniques that can be helpful in attaining a more quantitative understanding of the dynamics of dislocations, interfaces, and cracks. We have reviewed the various possibilities of in situ TEM indentation, straining, and heating. The recently developed techniques of in situ TEM allows for

direct observation of indentation-induced dynamical processes, reversible motion of dislocations in ordered intermetallic compounds and crack blunting phenomena. The in situ TEM indentation, in situ TEM straining, and heating experiments are summarized as follows:

The appearance of discrete yield events during nanoindentation of metallic systems depends on the ability of dislocations to propagate into the crystal, and is therefore substantially affected by solute pinning. Under load control, the characteristic yield excursions commonly observed in pure metals are strongly attenuated by solute pinning, leading to a more continuous loading response. Under displacement control, pure metals mostly exhibit full load relaxation during discrete yielding, but in alloys, solutes impede dislocation motion and thereby prevent the load from relaxing completely upon reaching a plastic instability. Yield events are resolved more clearly under displacement control, particularly in the presence of solute drag, since displacement-controlled indentation does not require collective dislocation motion to the extent required by load-controlled indentation in order to resolve a yield event. This perception is confirmed by in situ TEM displacement-controlled indentations, which show that many dislocations are nucleated *prior* to the initial macroscopic yield point and that the macroscopic yield event is associated with the *rearrangements* of the dislocations.

During indentation of the ultrafine-grained Al film, extensive movement of both low- and high-angle grain boundaries is observed. The occurrence of this deformation mechanism, which under uniform stress conditions is restricted to nanocrystalline materials, is attributed to the high-stress gradients involved in sharp indentation. In contrast to the observations in pure Al, no such movement of high-angle grain boundaries is found in any of the Al alloy films.

In coarse-grained Al–Mg alloys, superplastic deformation is accomplished by viscous glide of dislocations. The viscous glide is accompanied by dynamic reconstruction of the microstructure, the appearance of which depends on the deformation parameters and can be both detrimental and beneficial to the ductility. During dynamic recovery, grain refinement occurs by the formation of subgrain boundaries and low-angle grain boundaries. An advantage of plasticity based on viscous glide is that this mechanism has virtually no grain size dependence and therefore the preparation of such materials is less complex compared with the traditional fine-grained superplastic materials.

Intermetallic $D0_3$-based compounds show fully reversible dislocation motion in in-situ TEM straining experiments, i.e. plasticity induced pseudo-elasticity without a martensitic transformation. Emitting dislocations were observed from a crack tip providing support for the theoretical explanation that is based the motion of partial dislocations comprising superlattice dislocations.

In summary, new insights in the interaction between dislocations and planar defects such as grain boundaries in solution strengthened alloys and heterophase interfaces in intermetallic compounds have been achieved. It is concluded that with recent advances in in situ transmission electron microscopy the nucleation and propagation of cracks due to dislocation pile-ups can be scrutinized in self healing metallic materials.

Acknowledgements The authors are grateful to the support and collaboration with Wouter Soer (Philips Research), Yukichi Umakoshi (Osaka), Andy M. Minor, Eric A Stach, all from LBL Berkeley USA, with Steven Shan, SA Syed Asif, Oden L Warren, all from Hysitron, USA, and with Béatrice Doisneau-Cottignies, Grenoble, France.

References

1. Nabarro FRN (1967) Theory of crystal dislocations. Oxford University Press, Oxford
2. Hirth JP, Lothe J (1968) Theory of dislocations. McGraw-Hill, New York
3. Hall EO (1951) Proc Phys Soc Lond B 64:747
4. Petch NJ (1953) J Iron Steel Inst 174:25
5. De Hosson JTM, Kanert O, Sleeswyk AW (1983) In: Nabarro FRN (ed) Dislocations in solids. North-Holland, Amsterdam, pp 441–534
6. Wall MA, Dahmen U (1997) Microsc Microanal 3:593
7. Wall MA, Dahmen U (1998) Microsc Res Tech 42:248
8. Stach EA, Freeman T, Minor AM, Owen DK, Cumings J, Wall MA, Chraska T, Hull R, Morris Jr JW, Zettl A, Dahmen U (2001) Microsc Microanal 7:507
9. Minor AM, Morris Jr JW, Stach EA (2001) Appl Phys Lett 79:1625
10. Minor AM, Lilleodden ET, Stach EA, Morris Jr JW (2002) J Electron Mater 31:958
11. Minor AM, Lilleodden ET, Stach EA, Morris Jr JW (2004) J Mater Res 19:176
12. Doherty RD, Hughes DA, Humphreys FJ, Jonas JJ, Juul Jensen D, Kassner ME, King WE, McNelley R, McQueen HJ, Rollett AD (1997) Mater Sci Eng A 238:219
13. Winning M, Gottstein G, Shvindlerman LS (2001) Mater Sci Eng A 317:17
14. Van Swygenhoven H, Caro A, Farkas D (2001) Mater Sci Eng A 309–310:440
15. Van Vliet KJ, Tsikata S, Suresh S (2003) Appl Phys Lett 83:1441
16. Shan Z, Stach EA, Wiezorek JMK, Knapp JA, Follstaedt DM, Mao SX (2004) Science 305:654
17. Jin M, Minor AM, Stach EA, Morris Jr JW (2004) Acta Mater 52:5381
18. Larsson PL, Giannakopoulos AE, Söderlund E, Rowcliffe DJ, Vestergaard R (1996) Int J Solids Struct 33:221
19. Soer WA, De Hosson JTM, Minor AM, Stach EA, Morris Jr JW (2004) Mater Res Soc 795: U9 3 1
20. Soer WA, De Hosson JTM, Minor AM, Morris Jr JW, Stach EA (2004) Acta Mater 52:5783
21. De Hosson JTM, Soer WA, Minor AM, Shan Z, Stach EA, Syed Asif SA, Warren OL (2006) J Mat Sci 41:7704
22. Warren OL, Downs SA, Wyrobek TJ (2004) Z Metall 95:287
23. Minor AM (2002) Ph.D. thesis, University of California, Berkeley
24. Mondolfo LF (1979) Aluminum alloys: structure and properties. Butterworth, London, p 313
25. Dahmen U, Westmacott KH (1988) Scripta Metall 22:1673
26. Schlagowski U, Kanert O, De Hosson JTM, Boom G (1988) Acta Metall 36:865
27. De Hosson JTM, Kanert O, Schlagowski U, Boom G (1988) J Mater Res 3:645
28. Detemple K, Kanert O, De Hosson JTM, Murty KL (1995) Phys Review 52 B:125
29. Nabarro FRN (1975) in: Hirsch PB (ed) The Physics of metals, vol 2. Cambridge University Press, Cambridge, p 152
30. Foreman AJE, Makin MJ (1966) Philos Mag 14:911
31. Kocks UF (1966) Philos Mag 14:1629
32. De Hosson JTM, Alsem WHM, Tamler H, Kanert O (1983) In: Sih GC, Provan JW (eds) Defects, fracture and fatigue. Martinus Nijhoff, The Hague, p 23
33. De Hosson JTM, Soer WA, Minor AM, Shan Z, Syed Asif SA, Warren OL (2006) Microsc Microanal 12(S02):890
34. Gane N, Bowden FP (1968) J Appl Phys 39:1432

35. Kramer DE, Yoder KB, Gerberich WW (2001) Philos Mag A 81:2033
36. Gouldstone A, Koh HJ, Zeng KY, Giannakopoulos AE, Suresh S (2000)Acta Mater 48:2277
37. Gerberich WW, Venkataraman SK, Huang H, Harvey SE, Kohlstedt DL (1995) Acta Metall Mater 43:1569
38. Gerberich WW, Nelson JC, Lilleodden ET, Anderson P, Wyrobek JT (1996) Acta Mater 44:3585
39. Bahr DF, Kramer DE, Gerberich WW (1998) Acta Mater 46:3605
40. Minor AM, Shan Z, Stach EA, Syed Asif SA, Cyrankowski E, Wyrobek T, Warren OL (2006) Nat Mater 5:697
41. Soer WA, De Hosson JTM, Minor AM, Shan Z, Syed Asif SA, Warren OL (2007) Applied Phys Lett (submitted)
42. Johnson KL (1985) Contact mechanics. Cambridge University Press, Cambridge
43. Larsson PL, Giannakopoulos AE, Söderlund E, Rowcliffe FJ, Vestergaard R (1996) Int J Solids Struct 33:221
44. Sickafus K, Sass SL Scripta Metall 18:165
45. Lin CH, Sass SL Scripta Metall 22:735
46. Rittner JD, Seidman DN (1997) Acta Mater 45:3191
47. Frank FC (1950) Plastic deformation of crystalline solids office of naval research. Washington, DC, p 151
48. Read WT (1953) Dislocations in crystals. McGraw-Hill, New York
49. Sutton AP, Balluffi RW (1995) Interfaces in crystalline solids. Clarendon Press, Oxford
50. Grimes R (2003) Mater Sci Technol 19:3
51. Underwood EE (1962) J Metals 14:914
52. Backofen WA, Turner IR, Avery DH (1964) Trans Am Soc Metals 57:980
53. Chokshi AH, Mukherjee AK, Langdon TG (1993) Mater Sci Eng R 10:237
54. Higashi K, Mabuchi M, Langdon TG (1996) ISIJ Int 36:1423
55. E Usui, T Inaba, N Shinano (1986) Z Metall 77:179
56. Taleff EM, Lesuer DR, Wadsworth J (1996) Metall Mater Trans A 27:343
57. Taleff EM, Henshall GA, Nieh TG, Lesuer DR, Wadsworth J (1998) Metall Mater Trans A 29:1081
58. Yoshida H, Tanaka H, Takiguchi K, European Patent No 0846781
59. Woo SS, Kim YR, Shin DH, Kim WJ (1997) Scripta Mater 37:1351
60. Friedel J (1967) Dislocations. Pergamon press, Oxford.
61. Horiuchi R, Otsuka M (1972) Trans Jap Inst Metals 13:284
62. Oikawa H, Matsuno N, Karashima S (1975) Met Sci J 9:209
63. Weertman J (1975) J Appl Phys 28:1185
64. Mills MJ, Gibeling JC, Nix WD (1985) Acta Metall 33:1503
65. Henshall GA, Kassner ME, McQueen HJ (1992) Metall Trans A 23:881
66. Drury MR, Humphreys FJ (1986) Acta Metall 34:2259
67. Kubin LP, Veyssière P(1982) Electron Microsc 531
68. Pelissier J, Debrenne P (1993) Microsc Microanal Microstruct 4:111
69. Couret A, Crestou J, Farenc S, Molenat G, Clement N, Coujou A, Caillard D (1993) Microsc Microanal Microstruct 4:153
70. Messerschmidt U, Bartsch M (1994) Ultramicroscopy 56:163
71. Doisneau-Cottignies B (2005) private communication
72. Chezan AR, De Hosson JTM (2005) Mater Sci Forum 405–497:883
73. Chezan AR, De Hosson JTM (2006) Mater Sci Eng A410–411:120
74. Soer WA, Chezan AR, De Hosson JTM (2006) Acta Mater 54:3827
75. McQueen HJ, Knustad O, Ryum N, Solberg JK (1985)Scripta Metall 19:73
76. Gourdet S, Montheillet F (2000) Mater Sci Eng A 283:274
77. Gifkins RC (1976) Metall Trans A 7:1225
78. Eshelby JD, Frank FC, Nabarro FRN (1951) Phil Mag 42:351
79. Leibfried G (1951) Z Phys 130:214

80. Weertman J (1996) Dislocation based fracture mechanics. World Scientific, Singapore
81. Barenblatt GI (1962) Adv Appl Mech 7:55
82. Bilby BA, Cottrell AH, Swinden K (1963) Proc Roy Soc A272:304
83. Kooi BJ, Poppen RJ, Carvalho NJM, De Hosson JTM, Barsoum MW (2003) Acta Materialia 51:2859
84. Frank FC and Stroh AN (1952) Proc Phys Soc 65:811
85. Stroh AN (1954) Proc Roy Soc 223A:404
86. Stroh AN (1958) Philos Mag 3:597
87. Yasuda HY, Nakano K, Nakajima T, Ueda M, Umakoshi Y (2003) Acta Materialia 51:5101
88. Yasuda HY, Aoki M, Takaoka A, Umakoshi Y (2005) Scripta Materialia 53:253
89. Yasuda HY, Nakajima T, Nakano K, Yamaoka K, Ueda M, Umakoshi Y (2005) Acta Materialia 53:5343
90. Yasuda HY, Nakajima T, Murakami S, Ueda M, Umakoshi Y (2006) Intermetallics 14:1221